

RAPID CALCULATION OF THEORETICAL CMB ANGULAR POWER SPECTRA

MANOJ KAPLINGHAT, LLOYD KNOX AND CONSTANTINOS SKORDIS
Department of Physics, One Shields Avenue
University of California, Davis, California 95616, USA
Submitted to ApJ

ABSTRACT

We have developed a fast method for predicting the angular power spectrum, C_l , of the cosmic microwave background given cosmological parameters and a primordial power spectrum of perturbations. After pre-computing the radiation temperature and gravitational potential transfer functions over a small sub-space of the total model parameter space, the rest of the model space (six or more cosmological parameters and arbitrarily many primordial power spectrum parameters) is reached via rapid analytic and semi-analytic approximations which are highly accurate on all angular scales for which linear perturbation theory applies. A single power spectrum can be calculated in ~ 1 second on a desktop computer. We discuss applications to cosmological parameter estimation.

Subject headings: cosmology: theory – cosmic microwave background

1. INTRODUCTION

The anisotropy of the Cosmic Microwave Background (CMB) is proving to be a powerful cosmological probe. Measurements of its angular power spectrum can be used to tell us about the baryon density, dark energy density, the nature of the dark matter, the age of the universe and the primordial spectrum of perturbations generated in the inflationary era (Pryke et al. 2001; Netterfield et al. 2001; Lee et al. 2001; Wang et al. 2001; Knox et al. 2001).

A persistent challenge to the analysis is the large number of model angular power spectra (C_l) that must be calculated in order to understand the constraints the data place on parameter spaces with seven to ten or even higher dimensions. Here we present a fast, yet accurate, method for computing the C_l for a given model.

These model angular power spectra are the expectation values of the variance of spherical harmonic coefficients, a_{lm} , where $\langle a_{lm} a_{l'm'}^* \rangle = C_l \delta_{ll'} \delta_{mm'}$. The C_l depend on the density of dark matter, the fraction of this which is hot dark matter, the density of baryonic matter, the redshift of reionization of the intergalactic medium, the dark energy density, the dark energy pressure and the mean spatial curvature. These cosmological parameters influence the evolution of perturbations in the photon temperature. The C_l 's also depend on the statistical properties of the initial perturbations, possibly produced in an epoch of inflation. These initial conditions are described with the primordial gravitational potential power spectrum, $P(k)$.

The C_l can be calculated highly accurately because of the applicability of linear perturbation theory. Indeed, this is one of the reasons the CMB is such a powerful cosmological probe. One need only solve the linearized Einstein and relevant Boltzmann equations, which can be cast as a set of coupled ordinary differential equations. Early codes (e.g. Bond & Efstathiou (1984)) directly solved the whole hierarchy, up to some limiting multipole moment, of the photon temperature perturbation and could take tens of hours to calculate C_l for a single model.

Hu & Sugiyama (1995) introduced a semi-analytic approach which was much faster than the “whole hierarchy” Boltzmann codes of the day and with an accuracy around 10%. That accuracy could be improved, but only at the

expense of much slower performance.

The line-of-sight integration method for solving the linearized Einstein and Boltzmann equations (Seljak & Zaldarriaga 1996) greatly reduced the time required for calculation of accurate theoretical power spectra by bypassing the need to solve the whole hierarchy. Publicly available codes based on this method, mostly CMBfast (Seljak & Zaldarriaga 1996), have been the workhorses of all parameter-determination efforts to date. Despite its great speed, these analysis efforts have typically required months of running CMBfast.

Tegmark & Zaldarriaga (2000) introduced a high- ℓ / low- ℓ split in the calculation of C_l to exploit analytic approximations valid at high ℓ and insensitivity to certain parameters at low ℓ . With this split they were able to calculate a 7-dimensional grid of C_l 's with many fewer calls of CMBfast than would have been required for a brute-force calculation. By analytically correcting these for reionization effects and scaling the tensor and scalar power spectra with separate amplitudes they covered a 10-dimensional parameter space.

We use a similar high- ℓ / low- ℓ split to exploit the same analytic approximations as Tegmark & Zaldarriaga (2000). Our methods though have several advantages including reduced pre-compute time (~ 1 month reduced to ~ 40 hours), and ability to handle large numbers of primordial power spectrum parameters. We have performed extensive accuracy tests showing that our errors are smaller than cosmic variance errors for $l < 1000$. We achieve these advantages by storing the Fourier- and Legendre-transformed temperature perturbation transfer function (rather than C_l), using more efficient choices for grid parameters, and further use of (highly accurate) analytic approximations. We also have an option where all the low- ℓ effects are calculated with semi-analytic approximations, greatly reducing pre-compute times and storage requirements even further, as well as allowing for greater ease in incorporating new physical effects. Our software package is called the Davis Anisotropy Shortcut (DASh)¹.

¹

DASh can be downloaded from
<http://www.physics.ucdavis.edu/Cosmology/dash/>

DASH incorporates many approximations that have been presented elsewhere in the literature, and also some new ones. We present an approximate scaling for the polarization low- ℓ reionization feature, an improved approximation for the reionization damping factor and a generalization of the angular-diameter distance scaling which makes it accurate for all angular scales even in the presence of non-zero curvature. We also present improved semi-analytical approximations for the calculation of low- ℓ temperature spectra. These improvements enable a semi-analytical calculation of low- ℓ spectra to an accuracy better than 2% on average over a wide range of cosmological parameters (including curvature).

Although recent work has shown the exploration of these large model spaces to be possible without DASH, our method greatly reduces the required computer resources. As such it will allow for extension to more parameters including those needed to describe isocurvature components, or the dark energy pressure. A particularly straightforward extension would be to the number of parameters used to describe $P(k)$, beyond the usual two needed for the power-law description. A faster method also makes it possible to redo calculations to check for sources of systematic error.

A preliminary version of DASH has already been used for parameter estimation from CMB data (Knox et al. 2001). There we combined DASH with the Monte Carlo Markov Chain (MCMC) approach to Bayesian inference described in Christensen et al. (2001). The MCMC approach requires many fewer likelihood evaluations than a direct grid-based approach even for applications with only a handful of parameters, and generally becomes even more advantageous as the dimensionality increases further (Gilks et al. 1996). Others have used MCMC for cosmological problems (e.g. Verde & Spergel 2002) and we expect the technique to become widely used in cosmology.

CMB anisotropies are conveniently broken up into two different types: those which are simply projections of features on (or near) the last-scattering surface (early anisotropy) and those that are generated much more recently (late anisotropy). After reviewing some notation in Section 2 we discuss our computation of early anisotropies in Section 3. In Section 4 we describe the two different ways we compute late-time effects due to gravitational potential decay and reionization of the inter-galactic medium. In Section 5 we quantify the level of accuracy by comparing 6,823 models as calculated with DASH to those calculated with CMBfast. In section 6 we describe our calculation of polarization power spectra and the contribution from tensor perturbations. In Section 7 we consider extensions, for example to including lensing effects, and finally in Section 7 we conclude.

2. NOTATION

Before discussing the method we quickly review some notation. The temperature observed in direction $\hat{\gamma}$ observed from any point in space, \mathbf{x} , can be written as

$$T(\mathbf{x}, \hat{\gamma}) = \bar{T} + \Delta(\mathbf{x}, \hat{\gamma}). \quad (1)$$

For anisotropy sourced by scalar metric perturbations the Fourier-transformed temperature perturbation is azimuthally symmetric and can be expanded in Legendre polynomials as

$$\Delta(\mathbf{k}, \hat{\gamma}) = \sum_l (2l+1) (-i)^l \Delta_l(\mathbf{k}) P_l(\mu) \quad (2)$$

where $\mu = \hat{k} \cdot \hat{\gamma}$. The multipole moments of the Fourier-transformed temperature perturbation can be written as $\Delta_l(\mathbf{k}) = \Psi_i(\mathbf{k}) \Delta_l(k)$ where $\mathbf{k} = k\hat{k}$ and $\Psi_i(\mathbf{k})$ is the perturbation in the gravitational potential (Ma & Bertschinger 1995) at some very early time when all relevant perturbation wavelengths are larger than the horizon. Note that when we write $\Delta_l(k)$ with a scalar rather than vector argument (as we do throughout), we are using it as a transfer function.

If we solve for $\Delta_l(k)$ assuming adiabatic initial conditions with $\Psi_i(\mathbf{k}) = 1$, then if we assume the perturbations are statistically isotropic and homogeneous we can calculate C_l for any arbitrary initial potential power spectrum $P(k)$ as

$$C_l = (4\pi)^2 \int_0^\infty dk k^2 \Delta_l^2(k) P(k) \quad (3)$$

where C_l is defined by

$$\langle a_{lm}(\mathbf{x}) a_{l'm'}^*(\mathbf{x}) \rangle = C_l \delta_{ll'} \delta_{mm'} \quad (4)$$

and

$$a_{lm}(\mathbf{x}) = \int d\hat{\gamma} Y_{lm}(\hat{\gamma}) \Delta(\mathbf{x}, \hat{\gamma}). \quad (5)$$

We often express densities in units of the critical density for $h = 1$ where $H_0 = 100h \text{ km sec}^{-1} \text{ Mpc}^{-1}$ and the critical density is $\rho_c \equiv 3H_0^2/(8\pi G)$. Following convention, we refer to densities in these units with the symbol ω . The baryon density is ω_b , the dark matter density is ω_d , the matter density is $\omega_m = \omega_b + \omega_d$, and the dark energy density is ω_x . Note that $\omega_i = \Omega_i h^2$. These symbols all refer to present day densities. We define a curvature ‘‘density’’ as $\omega_K \equiv \Omega_K h^2 = (1 - \Omega_{\text{tot}}) h^2$ where $K = -1, +1, 0$ corresponds to an open, closed or flat universe respectively. With this definition the Friedmann equation at the present time becomes $h^2 = \sum_i \omega_i$. We assume that a fraction, f_h , of the dark matter is hot and that the rest is cold. We further assume that the dark energy is a cosmological constant, though we discuss an extension of DASH to $w_x \equiv p_x/\rho_x \neq -1$ models.

3. EARLY ANISOTROPIES

The dynamical processes at early times (e.g., acoustic oscillations of the baryon-photon fluid, Hydrogen and Helium recombination rates and Silk-damping) are governed only by ω_b , ω_m and f_h . Photon density matters as well, but this is well-determined from the FIRAS measurement of the CMB temperature as $T = (2.728 \pm 0.004) \text{ K}$ (95% confidence) (Fixsen et al. 1996). Dark energy parameters and the curvature radius are irrelevant since the dark energy density at early times was negligible (in most models, certainly for a cosmological constant) and the curvature radius at last-scattering was much larger than the horizon at that time.

The small number of parameters which are necessary for fixing the statistical properties of the CMB at early times and on small scales led Tegmark & Zaldarriaga (2000) to create a high- ℓ grid of angular power spectra with grid parameters, n_s , ω_b , ω_d and f_h . Although Ω_Λ and Ω_K do affect the projection of comoving length scales into angular scales, they do so in a particularly simple manner. With the grid constructed at fiducial values of $\Omega_K = \Omega_K^*$, $\Omega_\Lambda =$

Ω_Λ^* , they obtain C_l for non-fiducial values of the curvature via (Wilson 1982):

$$C_l(\Omega_K, \Omega_\Lambda, \omega_b, \omega_m, f_h) = C_l^*(\Omega_K^*, \Omega_\Lambda^*, \omega_b, \omega_m, f_h) \quad (6)$$

where $C_l \equiv l(l+1)C_l/(2\pi)$,

$$\tilde{l}/l = D_A^{z_{\text{peak}}}(\Omega_K^*, \Omega_\Lambda^*)/D_A^{z_{\text{peak}}}(\Omega_K, \Omega_\Lambda) \quad (7)$$

and D_A^z is the angular diameter distance to z and z_{peak} is the redshift where the visibility function peaks. In section 5 we derive Eq. 6 and also a version which does not rely on any small-angle approximation, as this one does.

Early anisotropy effects for DASH are also calculated via direct numerical solution of the linearized Einstein and Boltzmann equations over a grid of parameters. The key difference is that DASH stores the Fourier and Legendre-transformed photon temperature perturbation, $\Delta_l(k)$, instead of C_l . Because of this difference, our grid only needs to contain cosmological parameters, and not the primordial power spectrum parameters. The dimensionality of the grid is reduced (and with it the storage requirements) and flexibility is increased since we are no longer restricted to power-law descriptions of the primordial power spectrum. A typical use of DASH will first take tens of hours of computing the $\Delta_l(k)$ grid by a call of CMBfast (Seljak & Zaldarriaga 1996) for each grid point. Only after the entire grid is computed (we say “pre-computed”) can DASH produce angular power spectra in ~ 1 second, as advertised. Specifically, the grid is over parameters ω_b , ω_m and f_h at fixed values of $\Omega_K \equiv 1 - \Omega_{\text{tot}} = \Omega_K^*$, $\Omega_\Lambda = \Omega_\Lambda^*$ and $\tau = 0$. For reasons of algorithmic simplicity the current implementation requires the number of grid points for each grid parameter to be a power of 2. From this grid, we get C_l for any ω_b , ω_m , f_h and the primordial power spectrum $P(k)$ by performing multi-linear interpolation on the grid of $\Delta_l(k)$ and then the integral in Eq. 3. DASH can then get any C_l , accurate for $l \gtrsim 100$, in the model space of $\{\omega_b, \omega_d, \Omega_\Lambda, \Omega_K, P(k)\}$ via Eq. 6.

Grid boundary and finite grid-spacing effects can be minimized by an intelligent choice of the parameters. For example, instead of gridding uniformly in ω_m we grid uniformly in $\ln \omega_m$ which makes the interpolation error more uniform over the range of ω_m values. The uniformity of errors is desirable since if one holds the number of grid points fixed a parameterization that has more uniform errors has a smaller largest error. We discuss variable choice more in the next section.

4. LATE-TIME AND GEOMETRIC EFFECTS

Although we can use a low-dimensional parameterization of the early anisotropy, the late anisotropy is sensitive to additional effects and more cosmological parameters. The additional effects are due to geometry, the decay of the gravitational potential which occurs in the curvature or dark-energy dominated era, and Thomson scattering off of the free electrons in the re-ionized intergalactic medium.

We take two approaches to including these additional effects. One approach requires calculation of a second grid of $\Delta_l(k)$ (the “low- ℓ grid” which has more dimensions than the high- ℓ $\Delta_l(k)$ grid already described. The other relies solely on semi-analytic calculation for the late-time effects. The first we will refer to as gDASH and the second as sDASH. The sDASH is not completely grid-independent;

it relies on the high- ℓ $\Delta_l(k)$ grid as an accurate description of the photon perturbations at early times and sub-curvature scales. Below we first describe the semi-analytic calculation of the various effects and then the additional grid.

We model the radiation temperature transfer function as being modified by one additive factor and one multiplicative factor:

$$\Delta_l(k) = \Delta_l^{\text{ISW}}(k) + R_l(\tau)\Delta_l^{\text{early}}(k). \quad (8)$$

where $\Delta_l^{\text{early}}(k)$ is interpolated from the previously described grid, $\Delta_l^{\text{ISW}}(k)$ is the late-time contribution from the “Integrated Sachs–Wolfe” effect explained below and $R_l(\tau)$ is the reionization damping factor for late-time optical depth to Thomson scattering, τ . The resulting power spectrum can thus be written as

$$C_l = C_l^{\text{ISW}} + R_l^2(\tau)C_l^{\text{early}} + R_l(\tau)C_l^{\text{ISW-early}} \quad (9)$$

In the following subsections we describe how we calculate C_l^{early} (which gets geometric corrections), C_l^{ISW} , the $C_l^{\text{ISW-early}}$ cross term and $R_l(\tau)$.

4.1. Geometry

Although the curvature scale is larger than the horizon at last scattering, curvature does have effects on the early evolution of super-horizon size modes, which are unobservable at the time of last-scattering, but which have observational consequences now. That this is the case should not be surprising since it is impossible to map, without deformation, a space of zero mean curvature onto one with non-zero mean curvature. One can see this formally as a result of the fact that the eigenfunctions of the Laplacian are different in spaces of different curvature. We will always denote the eigenvalues of the Laplacian as k . One can further define a “wavenumber” in curved space as $\beta^2 = k^2 + K/r_{\text{curv}}^2$, where $r_{\text{curv}} = H_0^{-1}/\sqrt{|\Omega_K|}$ is the curvature radius. In the closed case, the spectrum of eigenvalues is discrete and βr_{curv} takes on only integer values. Further, $\beta r_{\text{curv}} = 1, 2$ are pure gauge modes (Bardeen 1980). The eigenfunctions of the Laplacian in curved space are the so-called hyperspherical Bessel functions. We will follow the definition and notation of Abbott & Schaefer (1986) for the hyperspherical Bessel function and denote them as $\Phi_\beta^l(\chi)$. At small distances and short wavelengths, $\Phi_\beta^l(\chi) = j_l(k\chi)$ and $k = \beta$. For more details on perturbation theory and CMB anisotropies in non-flat backgrounds we refer the reader to Kamionkowski & Spergel (1994); White & Scott (1996).

We take as our starting point for this calculation the $\Delta_l(k)$ already stored in the high- ℓ grid with fiducial parameter values $\Omega_\Lambda = \Omega_\Lambda^*$ and $\Omega_K = 0$. Recall that this grid is for the temperature perturbation *today* and not on the last-scattering surface. Calculating C_l from this grid for arbitrary Ω_Λ and Ω_K requires two steps. We must first correct for the effects of curvature at last-scattering, and then correct for how the projection from last-scattering to today has changed. As mentioned, curvature introduces a cutoff scale, k_{curv} , in the spectrum of Laplacian eigenvalues such that $k_{\text{curv}} = 1/r_{\text{curv}}, 0, \sqrt{8}/r_{\text{curv}}$ for $K = -1, 0, 1$. Our correction for the effect of curvature at the epoch of last-scattering is to introduce a cutoff in the integral over

k ; i.e., we define

$$C_l^g = (4\pi)^2 \int_{k_{\text{curr}}}^{\infty} dk k^2 \Delta_l^g(k)^2 P(k), \quad (10)$$

where the g superscript stands for “grid” and implies that the quantity in question has been obtained from the grid by interpolation. We have found that this simple approximation works very well. Note that $P(k)$ here is the power spectrum for the flat model. We then use C_l^g to calculate an intermediate angular correlation function $C^g(\theta)$ which then needs to be stretched to the correct angular diameter distance. For monopole (isotropic) sources emitting from a thin shell the shift is particularly simple (Wilson 1982):

$$\begin{aligned} C(\theta) &= C^g(\theta'); \\ \xi &\equiv 2 D_A^{z_{\text{peak}}}(0, 0) \sin(\theta'/2), \\ \sin(\theta/2) &= \sinh_K(\xi/2) / D_A^{z_{\text{peak}}}(\Omega_K, \Omega_\Lambda). \end{aligned} \quad (11)$$

The function $\sinh_K(x)$ is defined as $\sin(x)$, x , $\sinh(x)$ for $K = 1, 0, -1$ respectively. Legendre-transforming the shifted $C(\theta)$ back to ℓ -space then gives us the C_l^{early} of Eq. 9.

The transformation of the correlation function is only exact for *monopole* sources on a thin shell at fixed redshift. The dipole source due to the peculiar velocities of the photon-baryon fluid, the thickness of the last-scattering surface, and late-time effects all violate these restrictions. We discuss the resulting (very small) errors in section 5.

At small angles ($\theta \ll 1$), Eq. 11 can be cast in terms of a shift in ℓ , as given by Eq. 6 (see section 5 for a derivation). Thus at small angular scales ($\ell \gtrsim 10$), a simple shift in ℓ is sufficient and one need not Legendre transform.

4.2. Gravitational Potential Decay

We now show how to calculate the C_l^{ISW} term and the $C_l^{\text{ISW-early}}$ cross term of Eq. 9. These result from the late-time generation of anisotropy due to gravitational potential (metric perturbation) decay. In linear perturbation theory gravitational potentials are independent of time when the Universe is completely flat and matter-dominated, but decay in the presence of curvature and/or dark energy. As CMB photons pass through the evolving potentials, new (secondary) anisotropy is created via what is called the Integrated Sachs-Wolfe (ISW) effect (Hu & Sugiyama 1995).

We calculate the ISW effect by evaluating the line-of-sight integral:

$$\Delta_l^{\text{ISW}}(k) = \int_{\eta_{\text{late}}}^{\eta_0} d\eta \Phi_\beta^l(\chi) S^{\text{ISW}}(k, \eta), \quad (12)$$

where η_0 is the conformal time today and $\chi = \eta_0 - \eta$. η_{late} is some late time prior to the onset of curvature domination or dark energy domination, which ever is earlier.

The ISW source term is:

$$S^{\text{ISW}}(k, \eta) = 2e^{-\tau(\eta)} \dot{\Psi}, \quad (13)$$

where the optical depth to Thomson scattering is given by

$$\tau(\eta) \equiv \int_{\eta}^{\eta_0} \dot{\tau} d\eta \quad ; \quad \dot{\tau} = \bar{n}_e \sigma_T a \quad (14)$$

where \bar{n}_e is the mean number density of free electrons and σ_T is the Thomson cross section. The visibility function is $g = \dot{\tau} \exp(-\tau(\eta))$. The gravitational potential Ψ is defined in Ma & Bertschinger (1995).

To calculate Ψ , when we make the grid of flat models we store not only $\Delta_l(k)$ but also $\Psi^g(k, z = 100)$. This we use as a transfer function, and then numerically solve for the growth factor, $D(z)$ so that

$$\Psi(k, z) = \frac{D(z)}{D(100)} \Psi^g(k, 100) \quad (15)$$

This factorization is possible because the evolution of non-relativistic matter perturbations is independent of k for modes inside or outside the horizon when the clustered components are pressureless (Heath 1977). For the growth function $D(z)$, we use the approximation given by Carroll et al. (1992).

For values of β smaller than some (l dependent) multiple of l/η_0 , we evaluate the intergral in Eq. 12 explicitly. For other values we use a generalization of the weak-coupling approximation of Hu & White (1996) which works best for large values of ℓ and β . Since $\Phi_\beta^l(\chi)$ is a rapidly varying quantity, one can take the source term out of the integral and evaluate it at the conformal time where $\Phi_\beta^l(\chi)$ attains its maximum ($\chi_{\text{max}} = \eta_0 - \eta_{\text{max}}$). This allows Eq. 12 to be written as:

$$\Delta_l^{\text{ISW}}(k) \simeq S^{\text{ISW}}(k, \eta_{\text{max}}) \int_0^{\eta_0} d\chi \Phi_\beta^l(\chi), \quad (16)$$

One is then left with the integral over the hyperspherical Bessel function whose solution can be written as a recurrence relation; we only need the values of the integral for $l = 0, 1$. Denoting the integral in Eq. 16 by I_β^l , the following recurrence relation can be derived:

$$I_\beta^l = -\frac{2l-1}{l} \frac{\Phi_\beta^l(\eta_0)}{\sqrt{\beta^2 - Kl^2}} + \frac{l-1}{l} \frac{\sqrt{\beta^2 - K(l-1)^2}}{\sqrt{\beta^2 - Kl^2}} I_\beta^{l-2} \quad (17)$$

For open and flat models analytical solutions can be written by taking η_0 to infinity; for closed models, we numerically evaluate I_β^l using Eq. 17.

Now we turn to the $C_l^{\text{ISW-early}}$ cross term. The largest correlation with late ISW comes from the Sachs-Wolfe (SW) effect. We currently neglect contributions from the primary Doppler and early ISW effects, though including them would improve the accuracy. The Sachs-Wolfe radiation temperature transfer function is given by $\Delta_l^{\text{SW}}(k) = [\Theta_0 + \Psi]^g(\eta_{\text{ISS}}) \Phi_\beta^l(\eta - \eta_{\text{ISS}})$, where “ISS” stands for Last Scattering Surface taken to be at $z = 1100$ and $[\Theta_0 + \Psi]^g(\eta_{\text{ISS}})$ is the effective photon temperature for the corresponding model interpolated from the high- ℓ grid. With $\Delta_l^{\text{early}} \simeq \Delta_l^{\text{SW}}$ thus calculated, we then get

$$C_l^{\text{ISW-early}} = (4\pi)^2 \int_{\beta_K}^{\infty} \beta^2 d\beta \Delta_l^{\text{ISW}} \Delta_l^{\text{early}} P_K(\beta), \quad (18)$$

where $P_K(\beta)$ is the curved space initial potential power spectrum (Zaldarriaga et al. 1998), and $\beta_K = 0, 0, 2/r_{\text{curr}}$ for $K = -1, 0, 1$.

4.3. Reionization

Thomson scattering smears out our view of the last-scattering surface, and therefore damps the early anisotropy. This damping is described by the reionization damping factor, $R_l(\tau)$. Our first step to calculating $R_l(\tau)$ is to extract it numerically from models in a grid (pre-computed

with multiple calls to CMBfast) over ω_b , ω_m , f_h and τ with $\Omega_K = 0$ and $\Omega_\Lambda = 0$. These models have no ISW effect so we simply set

$$R_l^2(\omega_b, \omega_m, f_h, \tau) = C_l(\omega_b, \omega_m, f_h, \tau) / C_l(\omega_b, \omega_m, f_h, 0). \quad (19)$$

As we will see later, at high ℓ $R_l^2 = \exp(-2\tau)$, so we actually extract F_l instead where $R_l^2 = F_l(1 - \exp(-2\tau)) + \exp(-2\tau)$. The F_l are stored as a function of $\ell/(\ell_r + 1)$ and we interpolate between the stored values to obtain the F_l for a target model with $\Omega_K = 0$, $\Omega_\Lambda = 0$. The reionization multipole is defined by $\ell_r = D_A^{z(\eta_r)}/\eta_r$, where η_r is the visibility function weighted conformal time (Hu & White 1997). As pointed out by Hu & White (1997), once we have R_l as a function of $\ell/(\ell_r + 1)$, it is not changed significantly by curvature or Λ or any other late time effect that happens *after* reionization. The R_l for arbitrary model parameters are thus given by $R_l(\Omega_K, \Omega_\Lambda) = R_l(0, 0)$ where $\tilde{l} = l(\ell_r(\Omega_K, \Omega_\Lambda) + 1)/(\ell_r(0, 0) + 1)$.

The reionization damping term $R_l^2(\tau)$ could also be obtained semi-analytically. Note that the source terms for the early anisotropy (not shown in Eq. 20) all get suppressed by $e^{-\tau}$, *independent* of ℓ . The ℓ -dependence of the damping factor comes entirely from the non-ISW late-time creation of anisotropy at low ℓ via a source term

$$S^{\text{RI}}(k, \eta) = g(\Theta_0 + \Psi) + \frac{2b_k}{3\Omega_m} \frac{d}{d\eta} \left[g \left(\dot{a}\Psi + a\dot{\Psi} \right) \right] \quad (20)$$

where a is the scale factor and $b_k \equiv (k^2 - 3K/r_{\text{curv}}^2)/k^2$. Thus

$$R_l^2(\tau) = \frac{C_l^{\text{RI}}(\tau) + e^{-2\tau} C_l^f(0)}{C_l^f(0)}, \quad (21)$$

where C_l^{RI} is calculated using $S = S^{\text{RI}}$ for $z < z_{\text{ri}}$ and $S = 0$ for $z > z_{\text{ri}}$.

In writing S^{RI} we have neglected the Doppler source term proportional to the difference in baryon and photon fluid velocities. For reasonable values of the baryon density, this late-time Doppler effect only starts to become important for $z_{\text{ri}} \gtrsim 25$ (Hu & White 1996).

We treat reionization as if it instantaneously occurred at $z = z_{\text{ri}}$. We use z_{ri} instead of τ , as the input to DASH, since z_{ri} is more directly related to observational constraints (Becker et al. 2001; Fan et al. 2001). When we sample parameter space in order to characterize the accuracy of DASH, as described in Section 5, we always keep $z_{\text{ri}} \leq 10$. For a review of theoretical work on reionization see Loeb & Barkana (2001).

4.4. A low- ℓ grid

We have also implemented in DASH a numerical calculation of the gravitational potential decay and geometrical effects with the pre-computation of a low ℓ $\Delta_l^2(k)$ grid. This second-grid approach, called gDASH, has the advantages of speed and tunable accuracy over sDASH.

The low- ℓ grid, due to its incorporation of the late-time effects, necessarily has more dimensions than the high- ℓ grid. We have chosen these extra variables to be Ω_Λ/Ω_m , since this combination controls the ISW effect and ω_K since this sets the curvature radius. The low- ℓ grid is *less* sensitive to f_h , ω_b and ω_m than is the case for the high- ℓ

grid so we can grid more coarsely in these (Tegmark & Zaldarriaga 2000).

Although ω_m has little effect on late-time generation of anisotropy, this parameter directly controls the amount of *early* ISW effect. Since the early ISW effect is not projected to us from the last-scattering surface, the angular scaling assumed for use of the early grid will introduce some errors. Fortunately, these errors are negligible and the late grid can indeed be fairly coarse in ω_m .

We join the results of the low- ℓ and high- ℓ calculations by simply using the low- ℓ calculation up to a limiting value l_{late} . Our algorithm for choosing l_{late} is derived from a combination of analytic expectation and experience. First we define

$$l_\Lambda = 40 \sqrt{\frac{|\Omega_\Lambda - \Omega_\Lambda^*|}{\Omega_m}}, \quad (22)$$

$$l_{\text{curv}} = \min \left[200 \left(\frac{\Omega_K}{\Omega_m} \right)^{1/3}, 120 \right], \quad (23)$$

with l_{curv} defined for $\Omega_K \geq 0$, and then we set $l_{\text{late}} = \max(l_{\text{curv}}, l_\Lambda)$. For closed models we set

$$l_{\text{late}} = \max \left[25(-\Omega_K)^{1/3}, l_\Lambda \left(1 - 4 \frac{\Omega_K}{\Omega_m} \right)^{-1} \right], \quad (24)$$

which takes into account the effect of both Λ and curvature.²

Our reasoning is that below l_{late} , ISW and curvature effects become important. In principal $l_s \equiv \pi/\theta_s$ is another important scale, above which acoustic modifications to the intrinsic temperature on the last-scattering surface become important. We avoid extending the late grid to $l > l_s$ because this allows us to grid coarsely in ω_b . Fortunately l_{late} is always less than l_s . We choose to make the switch at l_{late} instead of l_s so that the low- ℓ grid can be coarse in ω_m ; cutting at higher ℓ would require finer grids in ω_m to accurately describe the early ISW effect.

To calculate $\Delta_l(k)$ for the target model from our n -dimensional grid we first locate the 2^n grid points of the surrounding hypercube. Then for each of these 2^n $\Delta_l(k)$ vectors we spline-interpolate (and quadratically extrapolate where necessary) on to the k values of the target model. This step is necessary because the k values of the grid differ from grid point to grid point. A uniform set of k values is not desirable since different models have different k -spacing requirements for fixed accuracy specification. For closed models a uniform set of k values is impossible due to the discrete nature of the spectrum.

The grid is inefficient (in computing time and storage resources) if a lot of the grid points are for models which are far from observationally viable. Since we use rectangular grids, this means we would like to choose parameters such that their viable ranges are independent of the values of the other grid parameters. A systematic way to do this would be to use the eigenvectors of the parameter Fisher matrix for some particular experiment (Efstathiou & Bond 1999).

We have not pursued this grid efficiency systematically, but rather have made the physically motivated choice of ²

² For closed models in the second-grid approach we simply set $l_{\text{late}} = \max(40, l_\Lambda)$ which works well for the parameter range under consideration ($|\Omega_K| < 0.3$).

our low- l grid parameters as ω_b , $\ln \omega_m$, $\sqrt{\Omega_\Lambda/\Omega_m}$ and ω_K . Of course, even with this parameterization, we are still free to find the parameter eigenvectors. Perhaps doing so will further increase the efficiency of the grid and we may incorporate this in future DASH implementations. Not only will eigenvectors provide the advantage of a grid with a rectangular region of viable models, but there is also an advantage in having the well-determined parameter combinations decoupled from the poorly-determined combinations. Variations in the well-determined ones (over the range of their compatibility with data) are most likely to reproduce a highly linear response in C_l and thus would require very few grid points (only two if the response were exactly linear). Variations in the poorly-determined parameters will generate a *non*-linear response, but we will not need to model these responses as accurately so once again will not need many grid points.

5. ACCURACY

To characterize the accuracy of DASH we have compared a suite of thousands of models calculated using CMBfast and compared them with the same models as calculated by DASH. The CMBfast calculations were done with very dense k -spacing, effectively eliminating k -spacing as a source of error. The DASH calculation used the grids as described in Table 1. We created our suite of comparison models by first considering all possible models with parameter values $\omega_b = 0.0145, .018, .022, .028, \omega_d = .06, .09, .15, .2, \Omega_\Lambda = 0, 0.2, 0.4, 0.5, 0.6, 0.7, 0.8, \Omega_K = 0, \pm 0.01, \pm 0.05, \pm 0.13, \pm 0.21, \pm 0.27, z_{\text{ri}} = 0, 5, 10$ and $n = 0.95, 1, 1.05$ where n is the scalar power-spectrum power-law index. Of these models, those within the grid boundaries of Table 1 and having $0.3 < h < 1$ and a first acoustic peak with $160 < l < 280$ were placed in the comparison suite. The suite contains 313 models with $z_{\text{ri}} = 0$ and $\Omega_K = 0$, 937 models with $\Omega_K = 0$ and 6,823 models total. We refer to the differences between the two calculating tools simply as ‘differences’ rather than ‘DASH errors’ because some of the differences are due to errors in CMBfast. Also some errors result in no difference because they are common to DASH and CMBfast. We have not attempted the more challenging task of providing an absolute measure of accuracy.

The results are shown in Figure 2 for sDASH and Figure 3 for gDASH. In both figures we have shown the maximum and average differences for flat models (top panels), for flat models with reionization (middle panels), and for flat and curved models with reionization (bottom panels). One can see that in every case the rms differences are below 1% for $l \gtrsim 30$ for sDASH and $l \gtrsim 10$ for gDASH. The rms fractional difference (for $l < 1000$) is in all cases below the cosmic variance error of $\sqrt{1/l}$.

The size of the differences relative to cosmic variance is encouraging, but unlike cosmic variance the calculational errors that give rise to these differences may be correlated from l to l . Therefore the target level is closer to $1/l$ than $\sqrt{1/l}$ (see Knox et al. (1998) and Efstathiou & Bond (1999)) since $1/l$ is the cosmic variance error on a band of C_l of width l . At all l values, DASH either meets this more conservative criterion or has sub-percent level differences with CMBfast.

DASH errors are certainly small enough to be insignif-

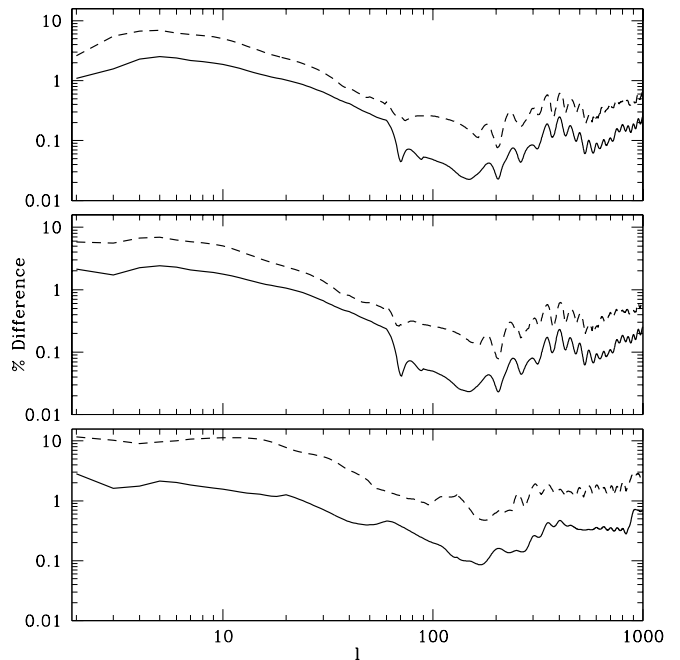


FIG. 1.— Differences between sDASH and CMBfast. Solid (dashed) lines show rms (maximum) percentage differences. The bottom panel is for all 6,823 models in the comparison suite (see text). The middle panel is for the 937 flat models in the suite. And the top panel is for the 313 flat models with $z_{\text{ri}} = 0$.

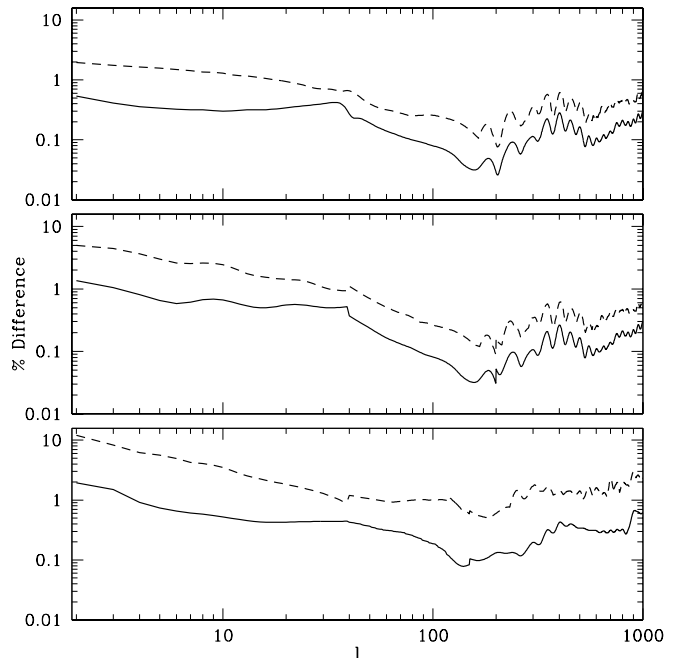


FIG. 2.— Differences between gDASH and CMBfast. See caption for Figure 1.

icant for parameter estimation from current data. But we do not yet understand the impact of sub percent level errors on parameter-determination from all-sky surveys such as the Microwave Anisotropy Probe (*MAP*)³. This is under investigation. The interpretation of the sub-percent level differences with CMBfast is complicated by the fact that the CMBfast calculation for some models can have percent level errors.

There are also errors due to neglect of non-linear effects. The most important of these are due to gravitational lensing and peculiar velocities of the reionized inter-galactic medium. We discuss including these effects in the Extensions section.

5.1. High l errors

At high l the top two contributors to error in the DASH calculations are interpolation error (at a level of about 0.5% by grid design) and error from the projection approximation. The chief cause of differences in the curved case is due to error in our CMBfast calculations arising from inaccuracies in the hyperspherical Bessel functions.

The projection approximation works remarkably well and we now turn to understanding that success. This can be seen from Figure 3 where we have plotted the differences between two flat models, shifted to correct for their 25% difference in angular diameter distance to the last scattering surface. Both the fiducial and target models in Figure 3 are flat and were calculated using CMBfast. Even for this large a shift, the errors at high l are $\lesssim 0.5\%$. We will argue that these differences must be due to numerical errors other than the projection approximation. We expect the projection to work just as well for curved models.

The scaling of $l(l+1)C_l$ with angular-diameter distance can be derived if one assumes the emission is from isotropic sources on an infinitesimally thin last-scattering surface. Then the correlation of temperatures at a given angular separation is equal to the correlation of temperatures on the last-scattering surface with a given physical separation. Therefore one can determine the angular correlation function of one model, from the angular correlation function of another, as long as both models have the same physical conditions before and at last-scattering. Specifically, spatial perturbations to the effective photon temperature monopole, $\Theta_0 + \Psi$, with angular correlation function $C(\theta)$ at angular diameter distance r , have correlation function $C'(\theta) = C(\theta r'/r)$ at angular diameter distance r' . The effect on the power spectrum is to have $C'_l \equiv l(l+1)C'_l/(2\pi) = C_l$, where $l' = r/r'l$ since:

$$\begin{aligned} C'_l &= l(l+1) \int d(\cos\theta) C(\theta r'/r) P_l(\cos\theta) \\ &\simeq l^2 \int \theta d\theta C(\theta r'/r) J_0(l\theta) \\ &= l'^2 \int dx x C(x) J_0(l'x) = C_{l'} \end{aligned} \quad (25)$$

where the approximation is accurate for $\theta \ll 1$.

We do not expect the thickness of the last-scattering surface to be a significant source of error. We find analytically that for thickness t and angular diameter distance d shifted to $d + \delta d$, the error in C_l is of the order

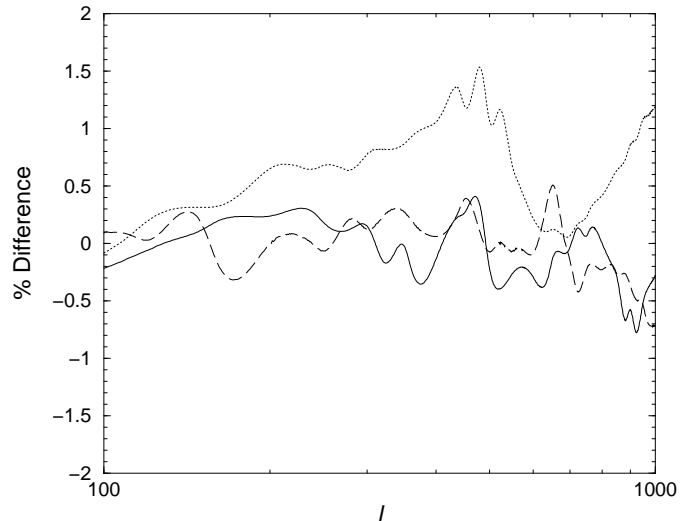


FIG. 3.— Projection errors for different components of the anisotropy. The target model is flat with $\Omega_\Lambda = 0.9$, $\omega_b = 0.02$ and $\omega_m = 0.12$, while the fiducial model is flat and has $\Omega_\Lambda = 0$. The ordinate shows the relative error (in %) for different components of the anisotropy produced at or close to the last scattering surface. The solid line shows the projection error for the total anisotropy, the dashed line for that of the Doppler contribution while the dotted line shows the error in projecting the ISW effect to the target model angular diameter distance.

$(\delta d/d)(t/d)^2 l^2 d^2 C_l / dl^2$ which is only important at the sub-0.1% level.

Anisotropies are generated soon after last scattering by the early ISW effect due to the decay of the gravitational potential in the presence of radiation. Thus for the early ISW effect there is a much thicker “last-scattering surface” and the projection approximation does not work as well as it does for the other early sources. However, the region in l space where the approximation is worst is also where it is a highly subdominant contribution to the total anisotropy.

Note that velocity perturbations on the last-scattering surface are a significant contribution to the anisotropy, and are not isotropic sources on the last-scattering surface. Velocity correlations in three-dimensions decompose into the correlation between components perpendicular to their separation vector and the components parallel to their separation vector. At small scales, the radial direction is nearly perpendicular to the separation vector and since the radial component is all that is important for the Doppler effect, we are primarily sensitive to the perpendicular component of the velocity correlation. This component projects like the monopole and the result is that dipole sources do not introduce much error, as can be seen in Fig. 3. At larger scales the parallel components of the velocity correlation also become important, but the velocity contribution is sufficiently small at larger angular scales that the resulting shifting errors are negligible.

A comparison of the open models to flat fiducial models using CMBfast shows that the high l shifting differences are much larger than the errors we expect analytically. The 1% to 2% differences are due to errors in the CMBfast calculation, presumably in the hyperspherical Bessel functions it uses. We compared the CMBfast outputs (at fixed ω_m and ω_b) for a flat model, a model with $\Omega_K = -0.002$

³

TABLE 1

GRID PROPERTIES

	$\sqrt{\Omega_\Lambda/\Omega_m}$	ω_K	$\ln w_m$	w_b	τ	total	$k_{\max}\eta_0$	n_k	n_l	Storage (Mb)
Low- l $\Delta_l^2(k)$	8	32	8	2	1	2,330	1600	1600	22	570
High- l $\Delta_l^2(k)$	1	1	32	8	1	256	6000	4500	60	250
F_l (reionization)	1	1	4	4	8	128	1600	1500	24	0.1
range	0:2.44	-0.15:0.16	$\ln(0.06) : \ln(0.28)$	0.01:0.03	0:0.3					

NOTES.—Entries in the middle rows to the left of the ‘total’ column show the number of values given for each parameter in the various grids. The ‘total’ column shows the total number of models in each grid. The low l total is less than the product of the other entries in the row because models that do not satisfy $0.1 < h < 1.1$ and $\Omega_m > 0$ and $0 \leq \Omega_\Lambda \leq 0.9$ are not calculated. All grids were given the same parameter ranges, shown in the bottom row. The High- l $\Delta_l^2(k)$ and F_l grids were evaluated at fixed $\Omega_\Lambda = 0.6$ and 0 (respectively), $w_K = 0$ and $\tau = 0$. The last four columns show the maximum k values, number of k values, number of l values calculated and the storage requirements (in Megabytes) for each grid.

and another with $\Omega_K = 0.001$. (All 3 models had $\Omega_\Lambda = 0$.) The differences in the angular diameter distances are less than 0.1% and hence we would expect very little difference in C_l . Instead we find 1–2% changes to C_l at high l between the flat and curved models, presumably due to difficulty in calculating the high l hyperspherical Bessel function accurately. Hence we conclude that projecting from a flat fiducial model to a curved target model is more accurate than the direct calculation using hyperspherical Bessel functions.

Although the current difference plots show we may not have met the more conservative criterion of having fractional errors below $1/l$, we are optimistic that we can get there. As data improve DASH will be able to improve along with them. Better data mean smaller viable regions of parameter space, so the grid boundaries can shrink, allowing for greatly decreased interpolation error without increasing the number of models in the grid. Projection errors, already small, will be further reduced since the shifts from the fiducial model will be smaller.

5.2. Low l errors

The gDASH can be made arbitrarily accurate at low l by decreasing the parameter grid spacing. This is not the case for sDASH where the accuracy is limited by the approximations made. Of course, even in the second grid method, decreasing the parameter grid spacings requires more computational resources, primarily in being able to pre-compute and store large number of $\Delta_l(k)$ files.

The default grid-spacings in DASH have been chosen so that the interpolation errors are $\lesssim 0.5\%$ at high- l . For low l , where percent accuracy is not important, the constraints imposed on the grid-spacings are more lenient. All the low l sDASH errors are due to interpolation.

The sDASH errors at $l < 10$ are larger than the gDASH errors. However, the conservative $1/l$ cosmic variance criterion is much easier to meet here. Maximum errors of the order of 10% can be tolerated. The maximum errors always come from the largest values of $|\Omega_K|$. A large part of the error is due to our approximate calculation of the

cross-term between the early contributions and the late ISW contribution. This could be improved as discussed earlier.

Another source of error in the semi-analytic calculations at very low l ($l \lesssim 5$) is the inability to carry out the projection as outlined in Eq. 11. Let r' and r be the coordinate distances to the last scattering surface of the target and fiducial models respectively. If $r' > r$, then there is no angle in the fiducial model that projects on to 180° in the target model. Hence one cannot obtain C_l by a Legendre transform. Choosing our fiducial model to be $\Omega_\Lambda = 0.6$ exacerbates this problem. However that choice for the fiducial Ω_Λ is justified by the aim of getting the high- l spectra very accurately for models close to the fiducial one. Note that choosing a non-zero Ω_Λ to be the fiducial model introduces another source of error into the low l semi-analytic calculations since one needs to subtract off the ISW contribution due to the fiducial Ω_Λ . The error introduced due to this is about the same as the error in calculating the flat models. One solution to these problems is to implement another high- l grid with $\Omega_\Lambda^* = 0$. This increases the pre-computing time and the storage requirements. We have not implemented this second grid but instead we approximate the projection effect and tolerate the error in the subtraction of the Ω_Λ^* ISW effect. For the projection, we use $l'(l' + 1) = l(l + 1) * r'^2/r^2$ to get to $l' = 4$ and then use the fact that at these large angular scales the spectrum is mostly sourced by the SW effect. Hence the lower multipoles can be obtained from $l' = 4$ by assuming that the ratio of C_l/C_4 is just given by the corresponding ratio of the integrals over the hyperspherical Bessel function squared times the power spectrum. We pre-compute these integrals assuming a scale-invariant power spectrum; deviations from scale-invariance are unlikely to be a significant source of error.

5.3. Speed

We used a personal computer with Pentium IV processors and version 2.96 of the GNU gcc g77 compiler for all our calculations. Computation of the high- l $\Delta_l(k)$

grid took ~ 4 hours, of the low- ℓ $\Delta_l(k)$ grid took ~ 40 hours and of the F_l grid took ~ 2 hours. After this pre-computing, gDASH requires 1.5 seconds and sDASH requires 2 to 3 seconds to calculate C_l . For comparison, CMBfast (with the same k_{\max} and n_k as used to precompute our grid—see Table 1) takes 50 seconds for flat models and about 90 seconds for $\Omega_K \neq 0$ models.

Significant time is spent reading the grid files each time a new model is computed. The grids we used (Table 1) could be stored in less than a Gbyte of RAM, and doing so may speed DASH up by a factor of two.

6. POLARIZATION AND TENSOR SPECTRA

The polarization power spectrum is calculated in DASH in a manner similar to the temperature spectrum. We store the polarization analogs of $\Delta_l(k)$ in the high- ℓ grid and use the same formulae for angular-diameter distance shifting and re-ionization suppression. The grid sizes for the polarization $\Delta_l(k)$ are smaller by about a factor of 2 because polarization $\Delta_l(k)$ is non-negligible over a smaller range of k for any given ℓ . The number of grid points required to achieve percent level accuracy is comparable to the temperature grid.

Reionization results in a new peak in the power spectrum at very low ℓ (Zaldarriaga 1997). It is the only important late-time effect; there is no analogous ISW effect for polarization. We have found a simple scaling relation that allows it to be calculated rapidly:

$$\begin{aligned} \mathcal{C}_{E'l} &= \mathcal{C}_{E*l} \frac{(1 - e^{-\tau})^2}{(1 - e^{-\tau_*})^2} \left(\frac{\tau_*}{\tau}\right)^{(0.2 - \tau_*/3)} \left(\frac{A}{A_*}\right) \left(\frac{2}{l_{\text{pivot}}}\right)^{n-1}, \\ \mathcal{C}_{C'l} &= \mathcal{C}_{C*l} \frac{(1 - e^{-\tau})}{(1 - e^{-\tau_*})} \left(\frac{\tau_*}{\tau}\right)^{0.2} \left(\frac{A}{A_*}\right) \left(\frac{2}{l_{\text{pivot}}}\right)^{n-1}, \end{aligned} \quad (26)$$

where \mathcal{C}_{El} is auto-correlation of the E (electric or scalar) mode of polarization and \mathcal{C}_{Cl} is the (E mode) polarization – temperature cross-correlation. The initial potential power spectrum is taken to be $P(k) = A (k/k_{\text{pivot}})^{n-4}$, and $l_{\text{pivot}} \equiv (6000 \text{ Mpc } k_{\text{pivot}})/(\omega_m(1 + z_{\text{ri}}))^{1/2}$. The angular diameter distance shifting is achieved through the relation $l' = l(l'_r/l_r)$ for \mathcal{C}_{El} and $l' = l(l'_r + 0.5)/(l_r + 0.5)$ for \mathcal{C}_{Cl} . The fiducial model, denoted by “*”, which we have used in our scaling relations has $\tau = 0.15$, $\omega_b = 0.02$, $\omega_m = 0.16$ and $\Omega_\Lambda = 0.65$. Since most of the optical depth to reionization is generated prior to the onset of curvature or dark energy domination there is no dependence on Ω_k or Ω_Λ . Also, since the relevant wavelengths are much larger than the horizon at last scattering there is no dependence on ω_b . Eq. 26 is accurate to $\sim 10\%$ near the peak of the reionization “bump”. When data warrant higher accuracy, a low ℓ grid can be created just as in the temperature case.

For the tensor temperature power spectrum, perturbations are continually generating temperature anisotropy along the line-of-sight so there is no useful late-time/early-time split and the simple angular-diameter distance projection corrections do not apply. However, a sufficiently accurate (3%) fit to the tensor temperature power spectrum already exists (Turner 1996) and we have included this in DASH. Note that polarization generation from tensor perturbations only occurs at last-scattering and after reionization so these could be included, when data warrant, in a manner analogous to the scalar case.

7. EXTENSIONS

There are a number of ways in which DASH could be extended. Additional effects can be included such as lensing, the Ostriker–Vishniac effect, patchy reionization, gravitational waves and dark energy with $p/\rho \neq -1$. DASH could also be extended to calculate the CMB polarization power spectra⁴.

Lensing of CMB photons by mass inhomogeneities on our past light cone leads to a smoothing of the power spectrum by a smoothing kernel $W_{l'}^l$ such that $C_l = \sum_{l'} W_{l'}^l C_{l'}$. This correction can be calculated rapidly and accurately as demonstrated by Zaldarriaga et al. (1998) who calculate it in real space. This smoothing by lensing is a very significant effect, leading to corrections at the several percent level at $l = 1000$ and tens of percent corrections at $l = 3000$ (Metcalf & Silk 1998). These corrections are useful because they break the curvature, Ω_Λ degeneracy (Metcalf & Silk 1998).

Above we have described how reionization generates new anisotropy on very large scales as photons pick up some of the peculiar momentum of the electrons via scattering. Although the linear theory contribution from this effect is very small at small angular scales, the second order contribution, called the Ostriker–Vishniac (OV) effect Ostriker & Vishniac (1986), can be the dominant source of anisotropy at $\ell \gtrsim 3000$. The OV contribution is $C_l \simeq 5\mu\text{K}^2$ according to a numerical calculation by Springel et al. (2001) and an analytic calculation by Ma & Fry (2001); also see recent forecasts for secondary anisotropy by Aghanim et al. (2002). Since it is primarily a second-order effect it is especially sensitive to the amplitude of the fluctuations and is therefore not sensitive to events at high redshift. In particular, since $z_{\text{ri}} > 6$ it is insensitive to z_{ri} . Semi-analytic means of rapidly calculating the power spectrum from the OV effect exist and could easily be included in DASH (Hu & White 1996; Jaffe & Kamionkowski 1998).

The transition from neutral IGM to ionized IGM is likely to go through a “patchy” period in which the two phases are spatially mixed. If patches of reionized IGM are small enough (comoving linear extent less than about 20 Mpc) then the first order contribution to anisotropy from scattering off of electrons does not experience cancellations and can be large (Aghanim et al. 1996; Gruzinov & Hu 1998; Knox et al. 1998). This contribution from patchy reionization is proportional to the redshift width of the transition and $(1 + z_{\text{ri}})^{3/2}$ (Gruzinov & Hu 1998). A small z_{ri} means that patchy re-ionization is almost certain to be subdominant compared to the non-patchy contribution (although see Aghanim et al. (2002) who assume a large typical patch size and find the patchy phase may contribute significantly).

The current implementation of DASH assumes the dark energy is a cosmological constant (i.e., $p = -\rho$). Whether the dark energy is a cosmological constant or not is a matter of profound importance in cosmology and fundamental physics. Dark energy models based on slowly-rolling scalar fields have $w \equiv p/\rho \neq -1$ and can in principle be observationally distinguished from a cosmological constant.

⁴

This has in fact already been done for a preliminary version of DASH (B. Gold, private communication)

The effect of dark energy on the CMB is solely gravitational; all we have to do is calculate how the dark energy affects Ψ . Ma et al. (1999) have shown that the effect of dark energy on the matter evolution can be factorized into one function of k and one function of time. We can use their fitting formulae for these functions to rapidly calculate Ψ at late times and therefore the ISW contribution to anisotropy.

8. CONCLUSIONS

We have described a fast and accurate method for calculating angular power spectra from the parameters of adiabatic models. Our implementation, DASH, is publicly available. Extensions for polarization, tensor modes and lensing are straightforward.

The speed of DASH will be useful for parameter estimation from CMB power spectrum data which typically requires more than hundreds of thousands of models to be calculated. DASH is particularly advantageous compared to grid-based C_l calculations for parameter estimation techniques which require calculation of C_l at random points in the parameter space, such as the MCMC method used in Knox et al. (2001) and described in Christensen et al. (2001). A preliminary version of DASH, valid only for flat models, was used in Knox et al. (2001). Since we pre-compute a transfer function instead of C_l DASH's advantage will be greatest for applications with large numbers of primordial power spectrum parameters—such as attempts to reconstruct this spectrum from data (Wang & Mathews 2000).

We are grateful to U. Seljak and M. Zaldarriaga for making CMBfast publicly available, S. Colombi, M. Tegmark and M. Zaldarriaga for useful conversations, and A. Kosowsky for his hyperspherical Bessel function routines. We used CAMB (Lewis et al. 2000) many times as we worked through various accuracy tests. LK thanks the IAP for their hospitality during early stages of this work. This work was supported by NASA grant NAG5-11098.

REFERENCES

- Abbott, L. F. & Schaefer, R. K. 1986, *ApJ*, 308, 546
Aghanim, N., Castro, P. G., Melchiorri, A., & Silk, J. 2002, *astro-ph/0203112*
Aghanim, N., Desert, F. X., Puget, J. L., & Gispert, R. 1996, *A&A*, 311, 1
Bardeen, J. M. 1980, *Phys. Rev. D*, 22, 1882
Becker, R. H., Fan, X., White, R. L., Strauss, M. A., Narayanan, V. K., Lupton, R. H., Gunn, J. E., Annis, J., Bahcall, N. A., Brinkmann, J., Connolly, A. J., Csabai, I., Czarapata, P. C., Doi, M., Heckman, T. M., Hennessy, G. S., Ivezić, *vz.*, Knapp, G. R., Lamb, D. Q., McKay, T. A., Munn, J. A., Nash, T., Nichol, R., Pier, J. R., Richards, G. T., Schneider, D. P., Stoughton, C., Szalay, A. S., Thakar, A. R., & York, D. G. 2001, *Astron. J.*, 122, 2850
Bond, J. R. & Efstathiou, G. 1984, *Astrophys. J. Lett.*, 285, L45
Carroll, S. M., Press, W. H., & Turner, E. L. 1992, *Annu. Rev. Astron. Astrophys.*, 30, 499
Christensen, N., Meyer, R., Knox, L., & Luey, B. 2001, *Classical Quantum Gravity*, 18, 2677
Efstathiou, G. & Bond, J. R. 1999, *Mon.Not.Roy.As.Soc.*, 304, 75
Fan, X., Narayanan, V. K., Strauss, M. A., White, R. L., Becker, R. H., Pentericci, L., & Rix, H. 2001, *astro-ph/0111184*
Fixsen, D. J., Cheng, E. S., Gales, J. M., Mather, J. C., Shafer, R. A., & Wright, E. L. 1996, *ApJ*, 473, 576
Gilks, W. R., S., R., & Spiegelhalter, D. J. 1996, *Markov Chain Monte Carlo in Practice* (London: Chapman and Hall)
Gruzinov, A. & Hu, W. 1998, *ApJ*, 508, 435
Haiman, Z. & Knox, L. 1999, in *ASP Conf. Ser.* 181: *Microwave Foregrounds*, 227
Heath, D. J. 1977, *Mon.Not.Roy.As.Soc.*, 179, 351
Hu, W. & Sugiyama, N. 1995, *ApJ*, 444, 489
Hu, W. & White, M. 1996, *Astron. & Astrophys.*, 315, 33
—, 1997, *ApJ*, 479, 568
Jaffe, A. H. & Kamionkowski, M. 1998, *Phys. Rev. D*, 58, 043001
Kamionkowski, M., Kosowsky, A., & Stebbins, A. 1997, *Physical Review Letters*, 78, 2058
Kamionkowski, M. & Spergel, D. N. 1994, *ApJ*, 432, 7
Knox, L. 1995, *Phys. Rev. D*, 52, 4307
Knox, L., Christensen, N., & Skordis, C. 2001, *Astrophys. J. Lett.*, 563, L95
Knox, L., Scoccimarro, R., & Dodelson, S. 1998, *Physical Review Letters*, 81, 2004
Lee, A. T., Ade, P., Balbi, A., Bock, J., Borrill, J., Boscaleri, A., de Bernardis, P., Ferreira, P. G., Hanany, S., Hristov, V. V., Jaffe, A. H., Mauskopf, P. D., Netterfield, C. B., Pascale, E., Rabii, B., Richards, P. L., Smoot, G. F., Stompor, R., Winant, C. D., & Wu, J. H. P. 2001, *Astrophys. J. Lett.*, 561, L1
Lewis, A., Challinor, A., & Lasenby, A. 2000, *ApJ*, 538, 473
Loeb, A. & Barkana, R. 2001, *Annu. Rev. Astron. Astrophys.*, 39, 19
Ma, C. & Bertschinger, E. 1995, *ApJ*, 455, 7
Ma, C., Caldwell, R. R., Bode, P., & Wang, L. 1999, *Astrophys. J. Lett.*, 521, L1
Ma, C.-P. & Fry, J. N. 2001, *astro-ph/0106342*
Metcalf, R. B. & Silk, J. 1998, *Astrophys. J. Lett.*, 492, L1
Netterfield, C. B., Ade, P. A. R., Bock, J. J., Bond, J. R., Borrill, J., Boscaleri, A., Coble, K., Contaldi, C. R., Crill, B. P., de Bernardis, P., Farese, P., Ganga, K., Giacometti, M., Hivon, E., Hristov, V. V., Iacoangeli, A., Jaffe, A. H., Jones, W. C., Lange, A. E., Martinis, L., Masi, S., Mason, P., Mauskopf, P. D., Melchiorri, A., Montroy, T., Pascale, E., Piacentini, F., Pogosyan, D., Pongetti, F., Prunet, S., Romeo, G., Ruhl, J. E., & Scaramuzzi, F. 2001, *astro-ph/0104460*
Ostriker, J. P. & Vishniac, E. T. 1986, *Astrophys. J. Lett.*, 306, L51
Pryke, C., Halverson, N. W., Leitch, E. M., Kovac, J., Carlstrom, J. E., Holzapel, W. L., & Dragovan, M. 2001, *astro-ph/0104490*
Seljak, U. & Zaldarriaga, M. 1997, *Physical Review Letters*, 78, 2054
Seljak, U. & Zaldarriaga, M. 1996, *ApJ*, 469, 437
Springel, V., White, M., & Hernquist, L. 2001, *ApJ*, 549, 681
Tegmark, M. & Zaldarriaga, M. 2000, *ApJ*, 544, 30
Turner, M. S. 1996, *Phys. Rev. D*, 53, 5727
Verde, L. & Spergel, D. N. 2002, *Phys. Rev. D*, 65, 043007
Wang, X., Tegmark, M., & Zaldarriaga, M. 2001, *astro-ph/0105091*
Wang, Y. & Mathews, G. 2000, *astro-ph/0011351*
White, M. & Scott, D. 1996, *ApJ*, 459, 415
Wilson, M. L. 1982, *Astrophys. J. Lett.*, 253, L53
Zaldarriaga, M., Seljak, U., & Bertschinger, E. 1998, *ApJ*, 494, 491
Zaldarriaga, M. 1997, *Phys. Rev. D*, 55, 1822